Opto-Electronic Advances

CN 51–1781/TN ISSN 2096–4579 (Print) ISSN 2097–3993 (Online)

Superchirality induced ultrasensitive chiral detection in high-Q optical cavities

Tianxu Jia, Youngsun Jeon, Lv Feng, Hongyoon Kim, Bingjue Li, Guanghao Rui and Junsuk Rho

Citation: Jia TX, Jeon Y, Feng L, et al. Superchirality induced ultrasensitive chiral detection in high-Q optical cavities. *Opto-Electron Adv* **8**, 250079(2025).

https://doi.org/10.29026/oea.2025.250079

Received: 15 April 2025; Accepted: 16 July 2025; Published online: 10 September 2025

Opto-Electronic Advances

Article

October 2025, Vol. 8, No. 10

DOI: 10.29026/oea.2025.250079 CSTR: 32247.14.oea.2025.250079

Superchirality induced ultrasensitive chiral detection in high-Q optical cavities

Tianxu Jia[1,2†], Youngsun Jeon[2†], Lv Feng[1], Hongyoon Kim[2], Bingjue Li[3], Guanghao Rui[1*] and Junsuk Rho[2,4,5,6*]

The scale mismatch between nanoscale biomolecules and sub-wavelength light hinders circular dichroism (CD) spectroscopy for chiral small molecule sensing. In this study, we propose a high quality-factor (Q-factor) optical cavity that offers a breakthrough solution to the intrinsic trade-off between optical chirality density and mode loss. A spin-preserving chiral metasurface utilizes bound states in the continuum (BIC)-guided mode resonance (GMR) degenerate modes to achieve a high Q-factor, while ensuring the preservation of chirality purity for circularly polarized light propagating within the cavity via spin-locking mechanism. Experimental results demonstrate that the BIC-GMR degenerate state enables near-perfect transmission CD up to 0.99, without requiring symmetry breaking. Full-wave simulations further predict that this synergistically enhanced system can achieve a Q-factor as high as 10037 and generate a localized field in the molecular interaction region with an optical chirality density enhancement of up to 400-fold, leading to 5025-fold amplification of the CD signal. This study establishes a foundation for detecting low-concentration chiral molecules, reveals high-Q enhancement, and advances chiral toward single-molecule sensitivity, opening new research avenues in chiral biosensing.

Keywords: superchirality; circular dichroism; Fabry-Pérot cavity; chiral metasurface

Jia TX, Jeon Y, Feng L et al. Superchirality induced ultrasensitive chiral detection in high-Q optical cavities. *Opto-Electron Adv* **8**, 250079 (2025).

Introduction

Circular dichroism (CD) spectroscopy is a crucial analytical tool for characterizing chiral materials and plays a key role in both fundamental scientific research and biomedical diagnostics[1–5]. Its core advantage lies in its ability to selectively recognize the spatial conformations of biomolecules, such as the secondary and tertiary structures of proteins, which exhibit distinct CD responses in the ultraviolet spectral region. This makes CD spectroscopy an invaluable method for protein conformation analysis, structural characterization, and the study of dynamic folding processes[6–8]. However, traditional CD spectroscopy faces technical limitations, particularly due to the scale mismatch between the characteristic size of

[1]Department of Optical Engineering, School of Electronic Science and Engineering, Southeast University, Nanjing 211189, China; [2]Department of Mechanical Engineering, Pohang University of Science and Technology (POSTECH), Pohang 37673, Republic of Korea; [3]School of Mechanical Engineering, Southeast University, Nanjing 211189, China; [4]Department of Chemical Engineering, Pohang University of Science and Technology (POSTECH), Pohang 37673, Republic of Korea; [5]Department of Electrical Engineering, Pohang University of Science and Technology (POSTECH), Pohang 37673, Republic of Korea; [6]POSCO-POSTECH-RIST Convergence Research Center for Flat Optics and Metaphotonics, Pohang 37673, Republic of Korea.

[†]These authors contributed equally to this work.

*Correspondence: GH Rui, E-mail: ghrui@seu.edu.cn; J Rho, E-mail: jsrho@postech.ac.kr

Received: 15 April 2025; Accepted: 16 July 2025; Published online: 10 September 2025

chiral molecules (on the nanometer scale) and the wavelength of light (on the order of hundreds of nanometers), resulting in weak signal intensities. As a consequence, practical applications often require high concentrations or large sample volumes, significantly restricting its use for trace sample analysis. Recent advancements in nanophotonics have provided promising solutions to this challenge[9–16]. In free space, the optical chirality density of left- and right-handed (LH and RH) circularly polarized light (CPL) is confined to $\pm C_0$ ($C_0 = \varepsilon_0 \omega \boldsymbol{E}_0^2/2$)[11]. Studies have shown that by controlling the optical chirality density (C) in the light field, a significant enhancement of molecular CD signals can be achieved. The increased light-matter interaction enabled by superchiral optical fields ($C/C_0 > 1$) provides a new technical approach to surpass the sensitivity limitations of traditional CD detection[12–16].

In free space, C is limited by the theoretical maximum of pure CPL and cannot be further enhanced. While nanostructures can provide local field enhancement, they inevitably introduce additional material absorption and scattering losses, referred to as mode losses, which lead to a reduced resonant Q-factor and a deterioration of the signal-to-noise ratio[2,3,13,17]. Recent developments in nanophotonic chiral sensing have opened multiple technological pathways[18–20]. At the material level, metals and dielectric materials exhibit complementary properties. Plasmonic metal structures[21–24] can achieve significant electric field localization at subwavelength scales through surface plasmon resonance, but their enhancement of the magnetic field is relatively limited, and the induced CD signals due to ohmic losses can interfere with the intrinsic CD signals of molecules. In contrast, high-refractive-index dielectric materials can simultaneously excite electric and magnetic multipolar modes via Mie resonances[25–28]. While their low-loss characteristics preserve the intrinsic CD signals of molecules, they are limited by weaker field localization effects. To overcome these challenges, researchers have leveraged the non-radiative properties of anapole states and the directional scattering conditions of the Kerker effect to enhance the intensity of superchiral fields by over two orders of magnitude[25–28]. Additionally, metal-dielectric hybrid systems have been developed for chiral detection applications. For instance, Mohammadi et al.[29] designed a silicon disk coupled with a metal nanorod structure, achieving a 300-fold superchiral field enhancement via gap modes. Jia et al.[30] developed an anapole-surface plasmon polariton strong coupling system that significantly improved the signal-to-noise ratio of molecular CD signals. Regarding structural design, traditional chiral nanostructures[15,22,23,31–34] (e.g., helical antennas, gammadion arrays) can generate strong optical chirality densities, but the background signals caused by their inherent chirality can severely interfere with the detection of weak molecular signals. Moreover, the complexity of these structures often necessitates advanced deposition techniques such as two-step photolithography, laser direct writing, or oblique-angle deposition[2,22]. In contrast, non-chiral nanostructures[14,24,27,35,36] —while capable of supporting superchiral near-field generation —do not produce the background CD signals associated with geometric chirality. Alizadeh and Reinhard[24] designed non-chiral plasmonic split-ring resonators that simultaneously excite electric and magnetic modes, resulting in a 15-fold enhancement in optical chirality density. Solomon et al.[25] used non-chiral silicon nanodisks to achieve a 138-fold increase in localized field optical chirality density under Kerker-like conditions. At the device level, the performance of single-layer nanostructures is limited by the finite light-matter interaction length. By constructing optical microcavities with multilayer configurations, the interaction path between chiral molecules and the optical field can be extended. Furthermore, through electromagnetic mode coupling enhancement mechanisms, CD signals can be amplified by 2 to 3 orders of magnitude. For example, Feis et al.[37] employed a silicon disk array to excite oblique incidence modes through first-order diffraction of the periodic array, thereby extending the optical path and enhancing the coupling between light and chiral molecules, resulting in an enhancement of the CD signal by more than two orders of magnitude. Scott et al.[38] simplified the cavity structure to achieve a three-order-of-magnitude increase in CD signal enhancement.

Regarding device performance optimization, the quality-factor (Q-factor) is the key parameter determining the efficiency of light-matter interaction enhancement and plays a critical role in achieving high-sensitivity detection[39]. For example, Hou et al.[40] achieved a CD enhancement of 0.8 by exciting high Q-factor (≈45) non-chiral surface plasmon polaritons in a plasmonic lattice and their interaction with chiral pores. To achieve even higher-order CD signal enhancement, it is essential to overcome the physical limitations between resonant mode losses and mode volume. The theory of bound states in the continuum (BIC), which offers theoretically

infinite Q-factors and extremely strong field localization, provides a breakthrough pathway. Mur-Petit et al.[41] were the first to demonstrate, via topological charge theory, that BIC modes can be achieved in chiral optical systems through symmetry control. Subsequently, various methods for implementing quasi-BIC through symmetry control have been proposed[42–46], such as bilayer metasurfaces designed based on mirror symmetry breaking, slanted etched nanorods, and double-gap split-ring structures. Notably, BIC-based sensors have shown advantages in high-spectral-resolution live-cell imaging, improving the resolution of traditional methods by one to two orders of magnitude. Recently, Rosas et al.[47] achieved strong transmission resonance in the mid-infrared range by controlling quasi-BIC modes in free-standing membrane metasurfaces and applied it to biosensing of monolayers of biomolecules. However, most existing studies focus on optimizing the electromagnetic characteristics of the quasi-BIC mode itself, while its synergistic mechanism with superchiral light fields has not been fully explored—especially in terms of how BIC confinement can enhance molecular CD signals, an area that remains under systematic investigation.

In this paper, we propose a new architecture for chiral resonators with high Q-factor, offering a breakthrough solution to the inherent conflict between the limited optical chirality density and mode losses in traditional CD detection. This resonator achieves topological protection of specific chiral optical fields by constructing chiral mirrors with spin-preserving reflection properties. Its unique design, which breaks geometric symmetry, not only utilizes BIC-guided mode resonance (GMR) degenerate modes to achieve high Q-factor but also ensures that CPL propagating within the cavity maintains chiral purity during multiple round trips via the spin-locking mechanism of the mirrors. Experimental results demonstrate that the proposed structure exhibits strong spin-selective transmission, achieving a transmission CD value as high as 0.99. Theoretically, it can support the formation of a Fabry-Pérot (F-P) cavity with a Q-factor exceeding 10^4 when used as a cavity mirror. Full-wave simulations further predict that the synergistic interplay between the BIC-GMR modes and the superchiral optical fields enables the generation of a homogeneous localized field in the molecular interaction region, enhancing the optical chirality density up to 400 times the free-space value C_0, and amplifying the molecular CD signal by a factor of approximately 5025. This innovative design paradigm of BIC chiral microcavities is poised to drive chiral spectroscopy detection technology toward single-molecule sensitivity, opening new avenues in chiral biosensing and chiral quantum optical devices.

Spin-preserving metamirror (SPM)

In a conventional F-P cavity constructed from high-reflectivity materials, the chirality of the light field is altered upon reflection within the cavity, as shown in Fig. 1(a-1). Consequently, the volume average C of the localized field within the cavity vanishes, resulting in no enhancement of the CD signal from chiral molecules inside the cavity. In contrast, a chiral optical cavity can preserve the spin state of the light field while ensuring efficient round-trip propagation. A crucial component of such a chiral cavity is the cavity mirror, which must possess both high reflectivity and spin-preserving characteristics, hence it is termed a SPM. This section will investigate the design principles of SPM and provide an in-depth analysis of its underlying physical mechanisms.

Design and performance of SPM

SPM can be realized through the break of all in-plane mirror symmetries as well as n-fold ($n \geq 2$) rotational symmetry is crucial[48,49]. As shown in Fig. 1(a-2), the unit structure of the metamirror comprises two elliptical holes and a central circular hole arranged on a square-lattice silicon nitride (SiN) photonic crystal plate. This configuration exhibits C_2 symmetry about the central axis of the circular hole, which is crucial for enabling the desired spin-preserving property. Besides, the dispersion curve of SiN from experimental data presented in Fig. 1(b) reveals a high refractive index with negligible loss for wavelengths beyond 345 nm. The structural parameters include a thickness H = 344.5 nm, a unit cell size P = 417 nm, D = 129 nm, d_x = 79 nm, d_y = 234 nm, C_x = 162.5 nm, C_y = 89 nm, which is designed for normally excitation with wavelength of 532 nm.

Transmission circular dichroism (TCD)[37] is used to explore the reflection property of the metamirror, which is defined as the transmittance (T) difference of the metamirror being excited by light with same polarization but different handedness, i.e. TCD = $(T^{-}-T^{+})/(T^{-}+T^{+})$, where the superscript + and – represent RH and LH, respectively. A metamirror with TCD close to 1 indicates that the structure can selectively achieve perfect reflection for RH and LH incident light, respectively. Figure 1(c) illustrate the simulated relation

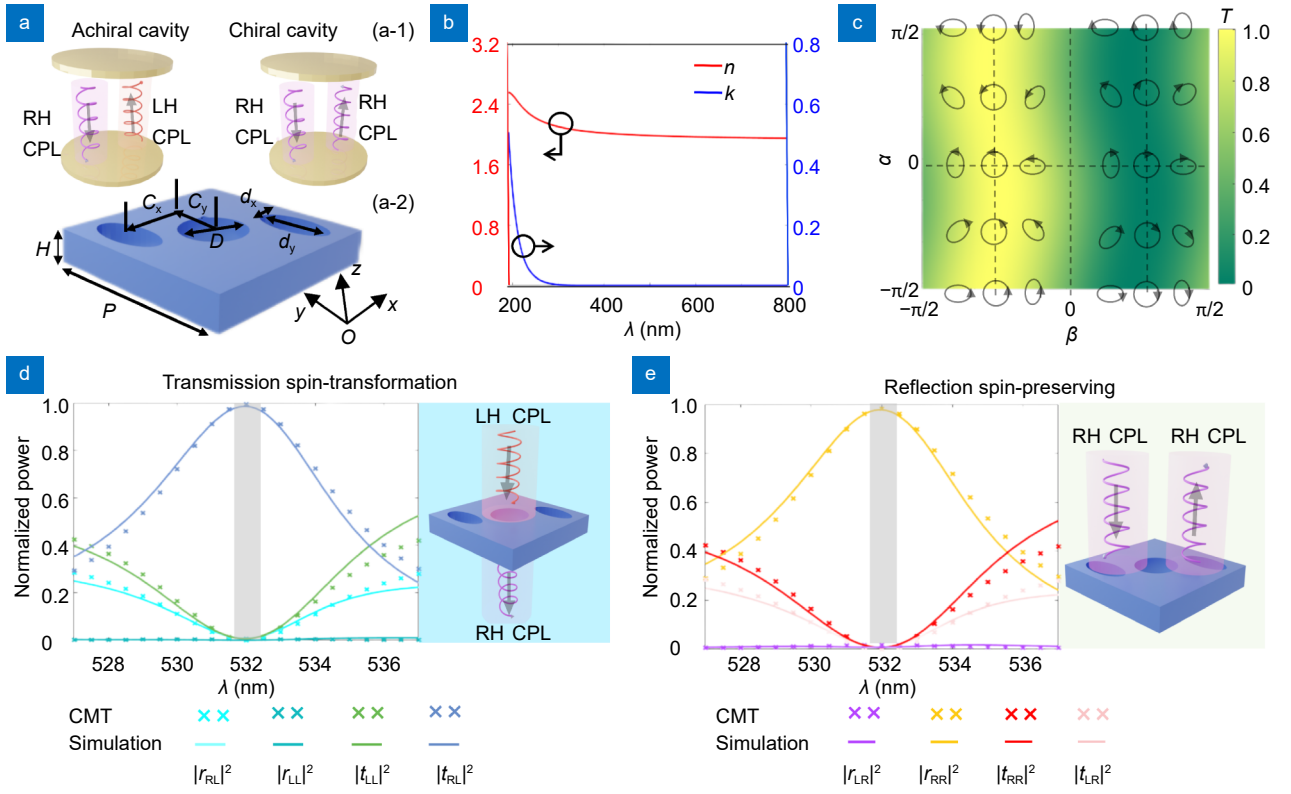

Fig. 1 | (**a**) The principles of chiral and achiral cavity (a-1) and the diagram of the proposed RH SPM (a-2). (**b**) Dispersion of SiN from experimental data. (**c**) Transmittance of the RH metamirror as a function of ellipticity β and azimuthal angle α of the polarization ellipse of the illumination. The states of polarization are indicated by the superimposed polarization ellipses. Normalized co- and cross-polarized reflection and transmission coefficients for RH metamirror excited by (**d**) LH CPL and (**e**) RH CPL light. The insets illustrate the optical response of the RH metamirror to incident CPL with different handedness.

between transmittance of the metamirror and the polarization state of illumination, which is in terms of azimuth angle α and ellipticity β of the polarization ellipse. The data were obtained from COMSOL Multiphysics simulations, and it can be seen that the transmittance is highly sensitive to the change in ellipticity. When $\beta = \pm\pi/4$ (corresponding to RH CPL and LH CPL respectively), the metamirror achieves near-perfect reflection for RH CPL with transmittance of 0.01, while maintaining near-perfect transparency for LH CPL with transmittance of 0.99, consequently leading to the TCD of 0.98. In contrast, the transmittance remains constant at 0.5 for linearly polarized light (corresponding to $\beta = 0$ or $\pm\pi/2$), which can be explained by the fact that linear polarization represents an equal superposition of RH CPL and LH CPL. Generally, the transmittance would diminish as the ellipticity decreases for most elliptically polarized states. It should be noted that high transmittance is not the sole criterion for selecting an appropriate excitation polarization state for the metamirror. For example, although the metamirror exhibits perfect transmission ($T = 1$) for LH elliptically polarized light ($\alpha = 5\pi/16$, $\beta = -9\pi/32$), its corresponding RH state ($\beta = 9\pi/32$) has a transmittance of only 0.04, giving rise to reduced TCD of 0.92 compared to circular polarization. Therefore, circular polarization is ultimately chosen as the excitation polarization state for the metamirror in this work.

Besides TCD, polarization characteristics of the reflected/transmitted light field is also essential for the design of SPM. Chiral coupled mode theory (CMT) provides a powerful framework for analyzing mode coupling phenomena[50,51] (as detailed in Section 1 of the Supplementary information). In this framework, the metamirror is characterized by a set of eigenstates described by a complex amplitude vector $\boldsymbol{p} = (p_1, \ldots, p_N)^{\mathrm{T}}$, and their temporal dynamics can be expressed as $\mathrm{d}\boldsymbol{p}/\mathrm{d}t = (\mathrm{i}\boldsymbol{\Omega} - \boldsymbol{\Gamma})\boldsymbol{p} + \boldsymbol{M}^{\mathrm{T}}\boldsymbol{a}$, where $\boldsymbol{\Omega}$ is the detuning between the eigenstate and the excitation frequency, $\boldsymbol{\Gamma}$ is the decay rate of the eigenstate, and $\boldsymbol{M}$ is the tensor of the coupling constant between the scattering channel and the eigenstate. Considering the metamirror is normally illuminated by a set of plane waves described by a complex amplitude

vector $\boldsymbol{a} = (a_{\mathrm{R}}, a_{\mathrm{L}}, a^{*}_{\mathrm{R}}, a^{*}_{\mathrm{L}})^{\mathrm{T}}$, where the variables with and without asterisks represent the amplitudes of incident waves from opposite directions. The interaction between the incident wave ($\boldsymbol{a}$) and the eigenstate ($\boldsymbol{p}$) determines the reflection and transmission amplitudes of the metamirror, collectively described by the scattering amplitude vector $\boldsymbol{b} = (b_{\mathrm{R}}, b_{\mathrm{L}}, b^{*}_{\mathrm{R}}, b^{*}_{\mathrm{L}})^{\mathrm{T}}$. The relationship between the incident and scattering fields is encapsulated in the scattering matrix ($\boldsymbol{S}$), which is the most important and carries the proportion of different spin components of reflected and transmitted light:

$$\boldsymbol{b} = \boldsymbol{S}\boldsymbol{a} = \begin{bmatrix} r_{\mathrm{RR}} & r_{\mathrm{RL}} & t^{*}_{\mathrm{RR}} & t^{*}_{\mathrm{RL}} \\ r_{\mathrm{LR}} & r_{\mathrm{LL}} & t^{*}_{\mathrm{LR}} & t^{*}_{\mathrm{LL}} \\ t_{\mathrm{RR}} & t_{\mathrm{RL}} & r^{*}_{\mathrm{RR}} & r^{*}_{\mathrm{RL}} \\ t_{\mathrm{LR}} & t_{\mathrm{LL}} & r^{*}_{\mathrm{LR}} & r^{*}_{\mathrm{LL}} \end{bmatrix} \boldsymbol{a}\,. \quad (1)$$

The amplitude of the scattering field can also be expressed as $\boldsymbol{b} = \boldsymbol{M}\boldsymbol{p} + \boldsymbol{C}\boldsymbol{a}$, where $\boldsymbol{C}$ represents the non-resonant scattering pathway. By solving for $\boldsymbol{p}$ and $\boldsymbol{b}$ under steady-state conditions, the scattering matrix $\boldsymbol{S}$ for the metamirror can be derived as $\boldsymbol{S} = \boldsymbol{C} - \boldsymbol{M}[\mathrm{i}\boldsymbol{\Omega} - \boldsymbol{\Gamma}]^{-1}\boldsymbol{M}^{\mathrm{T}}$ (refer to Section 1 of Supplementary information). By numerical simulation (indicated by solid lines "–") and using CMT fitting (indicated by symbol "×"), the results of the co- and cross-polarized reflectance and transmittance spectra of the CPL irradiated metamirror are shown in Fig. 1(d) and 1(e), in which t represents transmittance and r represents reflectance, with the first and second subscripts indicating the handedness of the reflected/transmitted and incident light, respectively. Remarkable agreement can be found between the fitting results and the simulation results, highlighting the robustness and accuracy of the analytical model. Importantly, it can be clearly seen that LH CPL would experience spin reversal ($|t_{\mathrm{RL}}|^2 = 0.985$) upon transmission through the metamirror at the wavelength of 532 nm, while RH CPL would maintain the original spin undergoing total reflection with $|r_{\mathrm{RR}}|^2 = 0.977$, demonstrating the ultra-efficiently spin-preserving property of the metamirror. Besides, CMT analysis enable us to evaluate the performance of the SPM. At the resonance wavelength of 532 nm, the fitted Q-factor of the SPM is around 168, which is an order of magnitude higher than the previously reported Q-factor of 43 for similar structure[48]. Notably, the SPM structure described above is termed a RH SPM. By taking its mirror image along the x-z plane, a LH SPM is obtained, which would reflect LH CPL while maintaining spin (refer to Fig. S2 of the Supplementary information).

BIC-GMR hybridization and spin-selective mechanisms in SPM

High Q-factor cavities serve as fundamental components for realizing ultra-sensitive chiral detection in optical microcavities. To unravel the physical origin of high Q-factor in SPM structures, the band characteristics and electric field distribution for like-TE eigenmodes are systematically analyzed. As shown in Fig. 2(a), both band-2 (brown curve, λ = 532 nm) and band-3 (green curve, λ = 519 nm) exhibit significant electric field localization effects at the Γ point in the first Brillouin zone, with their field intensities predominantly confined within the SPM structure. In contrast, band-1 (purple curve, λ = 532 nm) exhibits relatively weaker field confinement capabilities. Through correlating electromagnetic field localization characteristics with excitation modes and integrating Q-factor analysis from Fig. 2(b), band-1 with a Q-factor of 84 is identified as the GMR mode, which has limited oscillation duration due to energy loss. Remarkably, bands-2 and 3 display BIC characteristics with theoretically infinite Q-factors. However, the BIC mode at a wavelength of 519 nm remains unobservable under normal incidence conditions. Significantly, the spectral overlap between bands-1 and 2 at 532 nm creates a BIC-GMR hybridized mode through one-dimensional Dirac degeneracy at the Γ point. This modal degeneracy fundamentally enhances the Q-factor in SPM structures compared to conventional single GMR modes. It is worth noting that the present work significantly differs from previous studies on the realization of chiral optical responses based on BIC. For example, Shi et al.[46] proposed that quasi-BIC modes require oblique incidence or breaking in-plane geometrical symmetry to achieve the maximum optical chiral response for planar chiral metasurfaces. Differently, our results suggest that the maximum optical chiral response can be attained without symmetry breaking at the BIC-GMR degenerate mode, which provides a new idea for the design of chiral optical devices. To elucidate the degeneracy conditions between the BIC and GMR modes[52–54], a perturbation factor α_{δ} was introduced to modulate the structural parameters. The semi-major axes of the elliptical holes were adjusted in order to separately realize conditions involving the breaking of C_2 rotational symmetry and the mismatch between structural and design parameters (as detailed in Section 3 of the Supplementary information). The results demonstrate that C_2 rotational symmetry must be preserved to sustain the BIC mode, whereas precise parameter matching

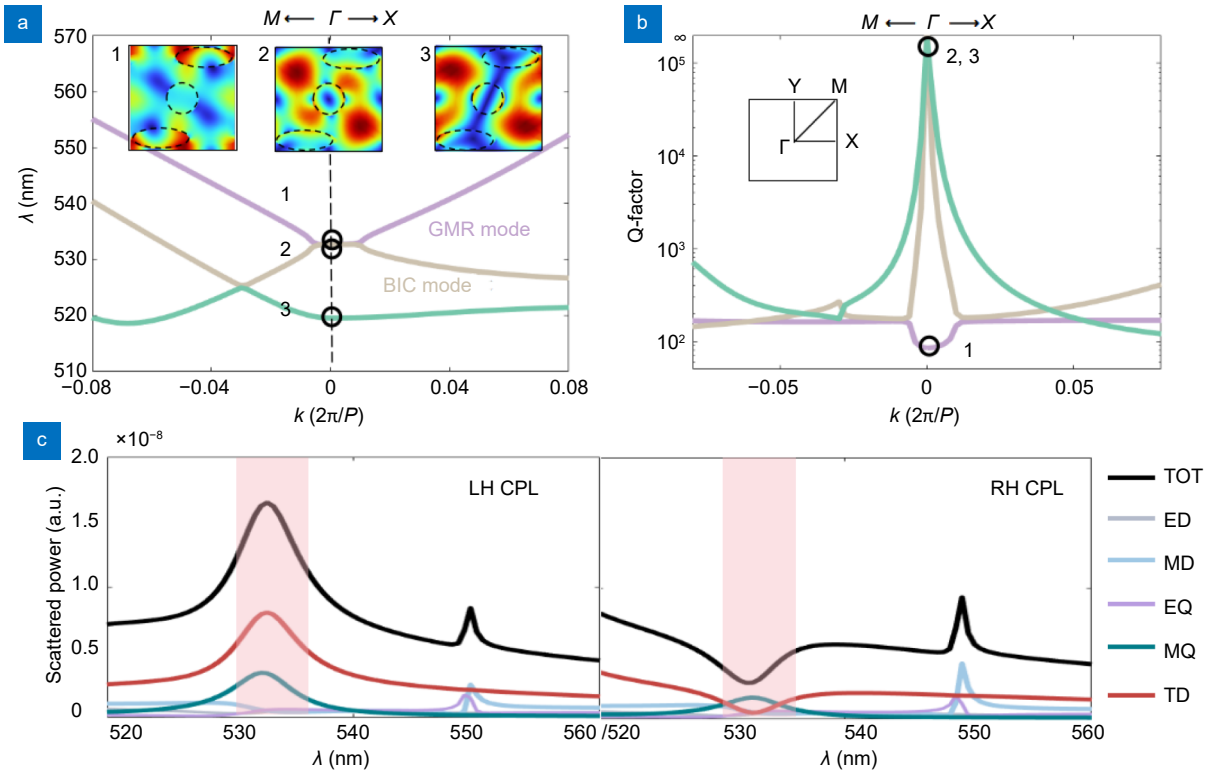

Fig. 2 | (**a**) Band structures of the SPM. The inset shows the magnitude distribution of electric field on *x*-*y* plane. (**b**) Q-factors corresponding to the band structures. (**c**) The scattering spectrum and multiple analysis of the SPM for LH CPL and RH CPL incidence. TOT: Total scattering; ED: Electric dipole; MD: Magnetic dipole; EQ: Electric quadrupoles; MQ: Magnetic quadrupoles; TD: Toroidal dipole.

is required to establish the BIC-GMR degenerate state.

To elucidate the spin-selective reflection mechanism inherent to SPM structures, scattering spectrum of SPM is calculated and presented by the black curve in Fig. 2(c). The structure exhibits maximal scattering contrast between LH CPL and RH CPL incident fields at 532 nm, manifested by a significant suppression of the total scattering intensity for RH CPL compared to LH CPL. This phenomenon persists stably within the 530–536 nm spectral range (pink-shaded region), while the scattering intensities of RH CPL and LH CPL converge outside this band. Through multipole analysis, the electric and magnetic excitations in the SPM structure were rigorously characterized. The scattering response is predominantly governed by contributions from TD mode, whereas contributions from ED, MD, and EQ modes are effectively suppressed. Notably, at 532 nm under LCP illumination, synergistic enhancement between the TD and MQ modes is observed, while TD response is markedly suppressed under RH CPL excitation. Consequently, the disparity in scattering intensities between TD and MQ modes under LH CPL and RH CPL illumination is identified as the key physical mechanism underlying the spin-preserved reflection in the SPM.

Experimental verification of the optical response of SPM

As the fabrication process shown in Fig. 3(a), the proposed SPM structure was carried out using electron beam lithography (EBL) and inductively coupled plasma (ICP) etching techniques (refer to Section 8 of Supplementary information for more details). The scanning electron microscope (SEM) images presented in Fig. 3(b) clearly show that the artificial micro-nano structures composed of circular and elliptical nanopores are arranged in a highly ordered periodic array, with each structural unit distinctly exhibiting geometric features. Furthermore, the experimental measurement of the linewidth of structure reveals a deviation from the theoretical design of less than 10%, indicating that the periodic precision and structural uniformity are highly accurate.

To verify the optical response characteristics of the SPM, an experimental setup was established for measuring spectral transmission (depicted in Fig. 3(c)), with the testing methods provided in the Section 8 of Supplementary information. The results indicate that the SPM

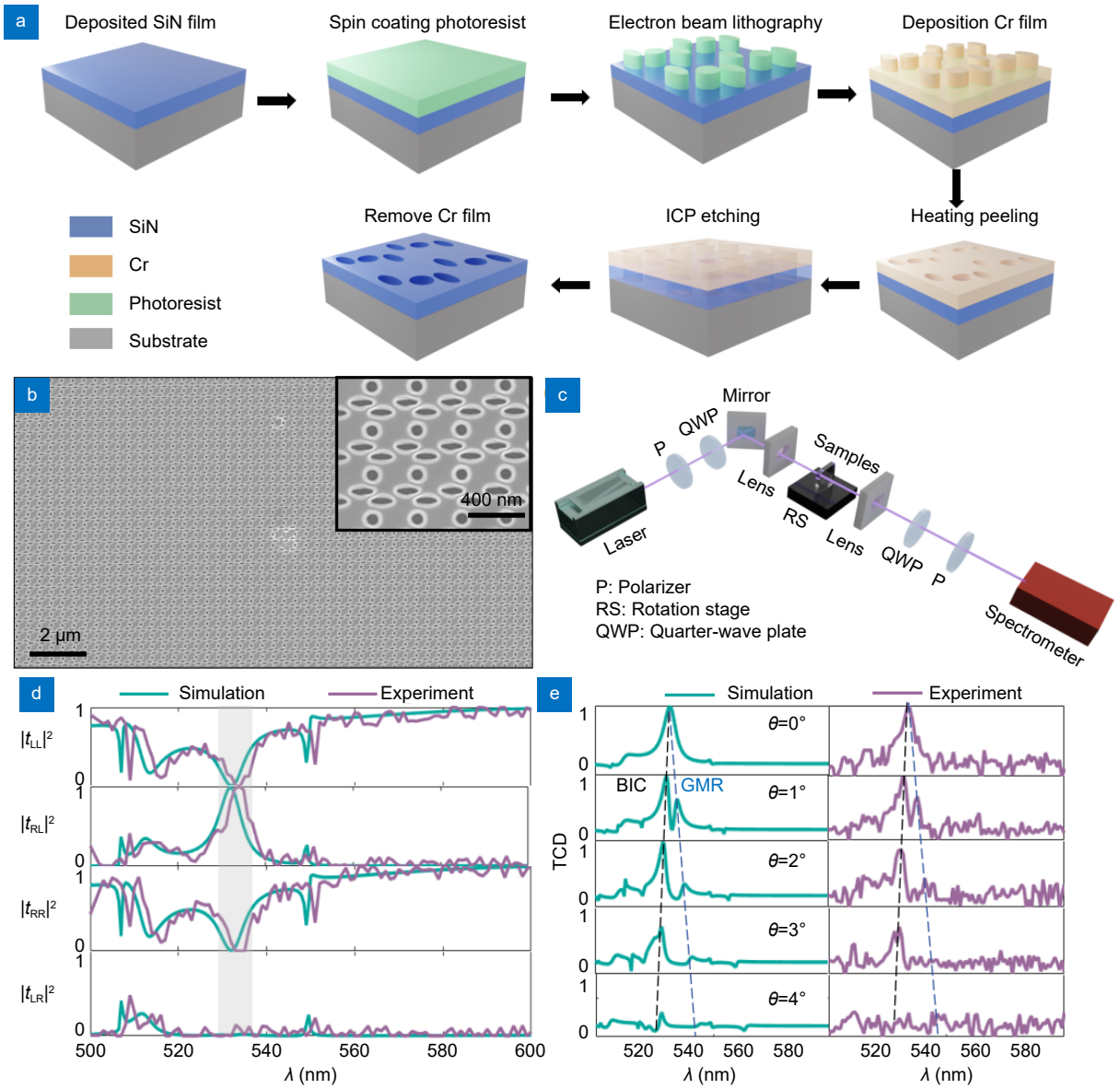

Fig. 3 | (**a**) Sample preparation. (**b**) SEM image of the fabricated SPM. (**c**) Experimental setup for spectra measurement under the circular polarization basis. (**d**) Simulated and measured transmission coefficients spectra for CPL with different handedness. (**e**) Simulated and measured TCD spectra for CPL with different incident angles.

demonstrates significant spin-selective transmission properties near the wavelength of 532 nm, with LH CPL being transmitted perfectly, while the transmission for RH CPL is almost zero (refer to Section 4 in the Supplementary information). Moreover, Fig. 3(d) compares the polarization characteristics of the transmission spectrum of SPM. Despite spectral jitter and shifts arising from fabrication accuracy and experimental errors, the overall spectral characteristics remain in good agreement with the theoretical predictions. Experimental results show that over most of the spectral range (e.g., 540–600 nm), CPL fields are efficiently transmitted while maintaining their original handedness. However, within the wavelength range of 530–536 nm (indicated by the gray shaded area), the SPM demonstrates efficient spin conversion characteristics for transmitted light. Considering the excitation wavelength of 532 nm, LH CPL would transmit and being converted to RCP by the SPM perfectly, with experimental/simulated values of $|t_{LL}|^2$ and $|t_{RL}|^2$ being 0.008/0.006 and 0.999/0.985, while RH CPL would be almost reflected by the SPM with experimental/simulated values of $|t_{RR}|^2$ and $|t_{LR}|^2$ being 0.002/0.006 and 0.002/0.008. Consequently, the corresponding Q-factor of SPM is approximately 150 (the theoretical value being 168).

Next, the effects of excitation angle on TCD spectrum of the SPM are investigated, with the experimental results for T^+ and T^- presented in Section 4 of Supplementary information. As illustrated in Fig. 3(e), the experimentally measured TCD spectrum aligns well with the theoretical results, with the peak value of TCD reaching 0.99 under normal incidence (the theoretical value being 0.98). As the incident angle increases to 4°, the resonance peak gradually splits into two modes: the BIC mode (shown by the black dashed line), which exhibits a blue shift accompanied by a broadening of the linewidth, and the GMR mode (shown by the blue dashed line), which displays a red shift and linewidth broadening. It is important to note that the TCD peak value is primarily dominated by the BIC mode, with simulated/experimental values of 0.87/0.93 (θ = 1°), 0.93/0.96 (θ = 2°), 0.69/0.66 (θ = 3°), and 0.33/0.25 (θ = 4°), thus indicating that the incident angle has a significant effect on the optical response of the SPM. Furthermore, based on a quantitative analysis of the relationship between structural deviations introduced during lithographic fabrication and the resulting shifts in resonance wavelength and variations in TCD intensity (refer to Section 4 of the Supplementary information), the observed resonance shift is primarily attributed to the reduction in the dimensions of the elliptical and circular holes.

Chiral optical cavity

Superchiral localized field generation

Figure 4(a) illustrates the construction of the chiral

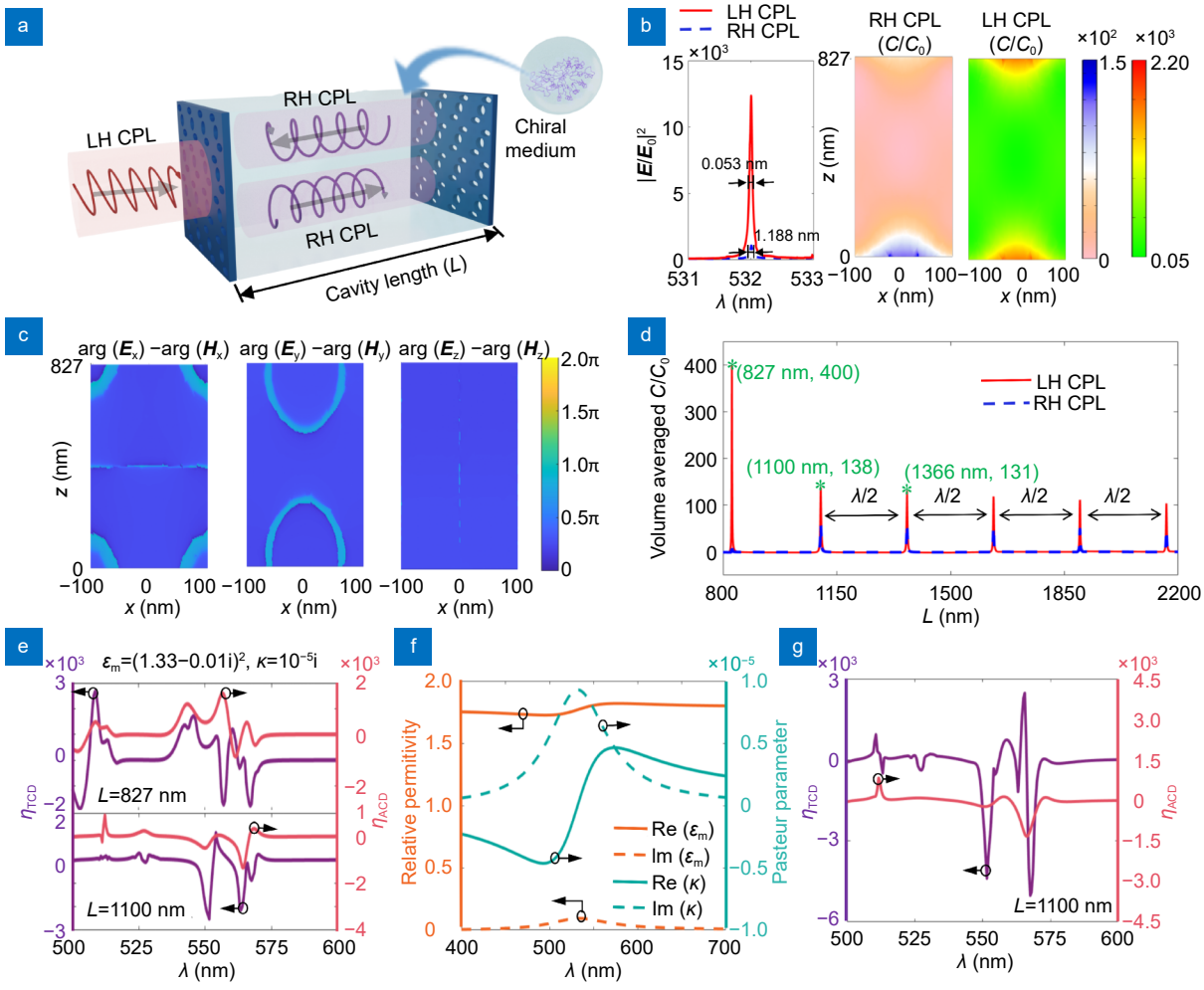

Fig. 4 | (**a**) Schematic of a chiral optical cavity with chiral medium. (**b**) The electric field enhanced spectroscopy and spatial profile of the superchiral field within the cavity excited by CPL. (**c**) Phase difference distribution between the parallel components of the electric and magnetic fields in the longitudinal plane. (**d**) Volume-averaged superchiral factor as a function of cavity length L. (**e**) Spectrum of η_{TCD} and η_{ACD} with varying cavity lengths. (**f**) Dispersion of the permittivity and chirality parameter of the chiral molecules. (**g**) Spectrum of η_{TCD} and η_{ACD} corresponding to the molecular parameters shown in (f).

optical cavity, which consists of a pair of SPMs with opposite handedness (i.e., a LH SPM and a RH SPM), where the central distance between these two SPMs is defined as the cavity length L. When LH CPL light is normally incident from above, LH SPM serves as the upper cavity mirror and exhibits a reflectance exceeding 98.5% for optical field with the same handedness, whereas approximately 0.8% of the transmitted field is converted into RH CPL light and subsequently enters the cavity. Since the lower cavity mirror is composed of a RH SPM, the transmitted light upon interacting with this mirror would undergo periodic handedness-matched reflection while propagating within the cavity, thereby forming a stable standing wave mode that significantly enhances the optical chirality density inside the cavity. In sharp contrast, RH CPL incident light, the transmitted field passing through the upper cavity mirror undergoes a conversion into LH CPL, and its transmission efficiency through the lower cavity mirror reaches 99.7%, which prevents the establishment of an effective standing wave and thus inhibits optical field enhancement within the cavity.

When the cavity length is precisely set to 827 nm, corresponding to approximately 1.56 times the working wavelength of 532 nm, Fig. 4(b) shows the electric field enhanced spectroscopy and the spatial distribution of superchirality factor. By using the Q-factor analysis method of electric field enhanced spectroscopy, the Q-factor of the chiral optical cavity reached a significant value of 10,037 under LH CPL excitation ($Q = \lambda_{peak} / \Delta\lambda$, λ_{peak} is the is the wavelength corresponding to the maximum value of electric field enhancement $|\boldsymbol{E}/\boldsymbol{E}_0|^2$, and $\Delta\lambda$ is the full width at half maximum of electric field strength). The corresponding local C enhancement at the interfaces of cavity mirror reaches three orders of magnitude, while the enhancement within the cavity region remains at two orders of magnitude. However, the Q-factor under RH CPL excitation is 448, and the superchiral field remains confined to the lower cavity mirror, whereas in other regions of the cavity the C enhancement remains below 20, indicating a highly selective optical response dependent on the handedness of the incident light.

To provide further insights into the underlying enhancement mechanism, we analyzed the phase difference between the parallel components of the electric and magnetic fields. As shown in Fig. 4(c), this phase difference closely approaches the ideal value of π/2 across most regions of the cavity, which represents the optimal condition for maximizing the optical chirality density of the local field. Additionally, the dependence of the C enhancement on the cavity length is presented in Fig. 4(d), it reveals that the volume-averaged superchiral factor exhibits periodic peak values when the cavity length satisfies an integer multiple of the half-wavelength, reaching a maximum of 400 at the optimal cavity length of 827 nm. However, as the cavity length increases to 1100 nm, this value drops significantly to 138. Notably, for cavity lengths exceeding 1.1 μm, each additional half-wavelength increments result in only a minor decrease of 7 in the volume-averaged superchirality factor, thereby ensuring a stable superchiral response over an extended range of cavity dimensions. To explain the sudden drop in the superchiral factor, a detailed analysis of the normalized $|\boldsymbol{E}|$ distribution at different cavity lengths was conducted, as presented in Section 5 of the Supplementary information. The results indicate that the significant superchiral factor observed at the cavity length of 827 nm originates from its unique oscillation mode, which is fundamentally distinct from the typical F-P resonance modes observed at other cavity lengths.

Enhancing CD signal with the superchiral field

To validate the enhancement effect of the superchiral localized field on chiral optical responses, a chiral solution was introduced into the resonant cavity to construct a coupled system, and the enhancement characteristics of TCD and absorption circular dichroism (ACD) were systematically investigated (refer to Section 6 in the Supplementary information for modelling method). In this study, ACD is defined as $ACD = (P^+ - P^-) / 2P_0$, where P^+ and P^- represent the total output power (including both transmitted and reflected components) under excitation of RH and LH CPL, respectively, and P_0 represents the incident power[33]. The enhancement factor $\eta_{TCD/ACD} = S_{net} / S_{bare}$ is defined as the ratio of the background-free net CD response (S_{net}) to that of the bare chiral solution (S_{bare}). Specifically, S_{net} is obtained by subtracting the cavity's CD response in the absence of chiral molecules (S_b) from the response in their presence (S_c) under identical solvent conditions, i.e., $S_{net} = S_c - S_b$. The chiral solution is characterized by a permittivity of $\varepsilon_m = (1.33-0.01i)^2$, permeability $\mu_m = 1$, and Pasteur parameters $\kappa = 10^{-5}i$. As illustrated by the purple curve in Fig. 4(e), when the cavity length is set to 827 nm, two distinct TCD enhancement dips are observed at wavelengths of 557 nm and 567 nm, where enhancement factors of

−1736 and −1776 were achieved, respectively. When the cavity length was further increased to 1100 nm, a slight blueshift of the resonance wavelengths was induced, which was accompanied by a marked increase in the enhancement factors, reaching −2520 at 551 nm and −2139 at 564 nm. Although both the ACD and TCD enhancement spectra were found to exhibit similar spectral characteristics under these conditions, it was also observed that the ACD response was notably limited due to the attenuation that occurred in the transmission channel. For instance, despite a TCD enhancement factor of −2139 being obtained at 564 nm, the corresponding ACD enhancement factor only reached −1331, which clearly indicated that the transmission channel imposed constraints on the achievable absorptive response. Furthermore, the influence of chiral medium dispersion on the detection performance is investigated, with the employed dispersion model provided in Section 6 of the Supplementary information and its spectral characteristics illustrated in Fig. 4(f). When the cavity length is fixed at 1100 nm, it is found that the overall spectral shape of the CD enhancement (shown in Fig. 4(g)) remained consistent with that of the non-dispersive case presented in Fig. 4(e), although slight spectral shifts were introduced. In particular, a maximum TCD enhancement factor of −5025 was recorded at 567.5 nm, whereas the ACD enhancement reached −1332 at a slightly blueshifted wavelength of 566 nm, thereby confirming that high enhancement performance could still be retained in dispersive media.

To further verify the robustness of the proposed model, we systematically investigated the influence of the solvent environment on both the resonance wavelength shift and the ACD response (refer to Fig. S8 in the Supplementary information). As the dielectric constant changes from that of pure water (ε_0 = 1.33[2]) to a high-concentration organic solvent (ε_0 = 1.36[2]), the system consistently maintains pronounced ACD enhancement, with values ranging from −1304 to −1005. Despite variations in the chemical composition of the chiral analyte, the cavity exhibits stable CD responses, demonstrating its ability to maintain strong signals and effectively tolerate environmental changes. Furthermore, the resonance wavelength exhibits high sensitivity to changes in the dielectric constant of the solvent, with each 0.01 increment in refractive index led to an approximate 1 nm redshift in resonance. These findings emphasize the exceptional sensitivity and tunability of the design, further confirming its potential as a reliable and versatile platform for chiral sensing applications.

Results and discussion

Currently reported SPM designs can be broadly classified into three categories, namely metallic, metal-dielectric hybrid, and all-dielectric structures[2,3,13,32,46,48,49,55]. While metallic and metal-dielectric hybrid SPMs typically exhibit low Q-factors and significant background noise, these limitations are primarily attributed to the intrinsic losses associated with the metallic components. For example, in the experimental study conducted by Kang et al.[55], a CD value of approximately 0.5 was reported, with a Q-factor of around 20, which was accompanied by considerable undesired background reflection. In contrast, dielectric SPMs are capable of achieving extremely high Q-factors with negligible background noise, particularly when the designs are driven by BIC modes

Table 1 | Representative nanophotonic approaches for chirality sensing.

Platform	Spectral region	Superchirality	CD enhancement	Ref.
Planar chiral metamaterials	Visible-Near IR (500–900 nm)	12#	/	ref.[7]
Gammadion gold array	Visible-Near IR (500–900 nm)	7#	180	ref.[15]
Helical plasmonic nanoantenna	Far IR (9–14 μm)	179#	/	ref.[33]
Titanium dioxide dimers	Near-Ultraviolet (350–400 nm)	125#, 80##	50	ref.[13]
Silicon dimers	Visible light (450–650 nm)	22#, 15##	20	ref.[14]
Born-Kuhn-type Gold dimers	Visible-Near IR (600–1100 nm)	/	3000	ref.[21]
Holey Silicon disks	Near IR (750–950 nm)	50#, 16##	24	ref.[57]
Silicon nanocylinders	Visible-Near IR (500–900 nm)	25#, 8##	300	ref.[58]
Cavity of Silicon disk arrays	Far IR (7.6–8.6 μm)	/	100	ref.[37]
F-P cavity of C_2 type (n = 4)	Near IR (790–810 nm)	1500#	/	ref.[48]
F-P cavity of Bragg reflector	Visible light (400–500 nm)	/	10-20	ref.[56]
F-P cavity of C_2 type SiN	Visible light (500–600 nm)	2200#, 400##	5025	This work

Note: "#" and "##" represents the superchirality factor of the maximum value and average value.

that can simultaneously support ultrahigh chiral responses and Q-factors. As demonstrated by Shi et al.[46], a planar metasurface capable of exciting quasi-BIC modes was designed to achieve a CD value as high as 0.99. However, such quasi-BIC modes generally require the intentional breaking of structural symmetry, which renders them unsuitable for constructing high-quality optical cavities. In the present work, a one-dimensional degeneracy between BIC and GMR modes is introduced, allowing us to overcome these inherent limitations while fully preserving the structural symmetry of the system. Consequently, both a high Q-factor and negligible background noise are simultaneously achieved. It should be emphasized that, although the present design and the SPM developed by Semnani et al.[49] both achieve spin-preserving reflection of CPL, the two approaches differ fundamentally in their underlying physical mechanisms and performance characteristics. In the previous design, the chiral response arises from GMR modes and structural asymmetry, which results in Q-factors below 100 and does not involve modal degeneracy. In contrast, the present design integrates BIC and GMR modes through a one-dimensional Dirac-point degeneracy, thereby enabling an experimentally measured Q-factor of 150 and a TCD approaching 0.99, while ensuring that full structural symmetry is maintained throughout the system. Furthermore, by constructing a chiral cavity based on this mirror, we achieve an approximately 400-fold enhancement in the volume-averaged optical chirality factor C, together with a substantially amplified CD response. These results reveal a design strategy wherein the synergistic combination of a high Q-factor, enhanced optical chirality, and strong field confinement paves the way for advancing both the capabilities and the application landscape of SPM in chiral photonics.

Furthermore, enhancing the asymmetric absorption of chiral molecules under CPL through the geometric chirality or electromagnetic modes of nanostructures has been recognized as a crucial strategy for overcoming the inherent limitations of CD detection, particularly in high-concentration samples[2,3]. In this study, the spin-preserving properties of cavity mirrors have been experimentally validated, which serve as a fundamental component of chiral resonant cavities. Besides, previous research[56] has incorporated a 100-nm-thick chiral thin film into a F-P cavity and result in a 10–20-fold enhancement of CD signal, supporting the feasibility of the chiral resonant cavity approach. Table 1 presents a comprehensive overview of representative nanophotonic approaches for chirality sensing. The significant amplification of CD signals through plasmonic chiral metasurfaces[7,15,33] has been attributed to the generation of additional chiral responses, such as plasmon-coupled CD arising from Coulomb interactions between chiral molecules and plasmonic structures. However, since this enhancement mechanism is prone to obscuring the intrinsic molecular signal, multiple measurements employing racemization techniques are typically required to disentangle molecular contributions. By contrast, achiral metasurfaces[13,14,21,57,58] has been shown to offer enhanced detection efficiency and cost-effectiveness in CD signal amplification, while the dielectric materials enabled the flexible tuning of operational wavelengths across the ultraviolet to infrared spectrum. Nevertheless, CD enhancement reported in most prior studies has been confined to within two orders of magnitude. In contrast, cavity-enhanced optical methodologies[37,48,56], which allow multiple optical passes within a resonant cavity, have been demonstrated to provide a highly effective means of amplifying weak chiral signals, leading to unprecedented sensitivity in absorption and birefringence measurements. In the present work, a chiral resonant cavity exhibiting the highest volume-averaged superchiral factor reported to date has been successfully constructed, thereby enabling the direct detection of molecular chirality while effectively mitigating interference from chemical modifications that could otherwise alter molecular activity. Moreover, even when compositional variations occur within the chiral medium, the system has been observed to maintain stable CD resonance peak recognition, thereby ensuring robust and universal detection capabilities across a broad spectrum of chiral analytes.

This breakthrough has been made possible by the synergistic contributions of three key factors. Firstly, the superior mechanical strength and lower optical loss exhibited by SiN have provided an optimal material platform for the realization of high-performance resonant structures. Secondly, the BIC-GMR hybrid mode has facilitated the achievement of an exceptionally high Q-factor in cavity mirrors, thereby introducing a novel physical paradigm for enhanced optical confinement. Finally, the incorporation of a chiral optical cavity structure has significantly extended the effective interaction length between the optical field and chiral molecules by enabling repeated photon circulation within the cavity. Furthermore, the integration of superchiral structures

with microfluidic channels is expected to enable high-throughput, real-time monitoring, thereby paving the way for transformative applications in drug screening and biosensing. It is important to note that the intrinsic chirality of the cavity inevitably introduces a non-negligible achiral background response alongside the enhanced chiral signal. Consequently, the signals generated by opposite enantiomers do not exhibit strictly anti-symmetric behavior, which limits the applicability of the cavity for accurate quantification of enantiomeric excess (refer to Fig. S9 in the Supplementary information). Nevertheless, the cavity supports distinct resonant modes under LH and RH CPL excitation. Even slight variations in the cavity composition can significantly affect the coupling efficiency and interference conditions, resulting in resonance dip shifts in opposite directions for the two enantiomers. Leveraging this mechanism, the proposed chiral cavity enables not only highly sensitive detection of trace chiral species but also reliable discrimination between R- and S-type configurations (refer to Section 9 in the Supplementary information).

Conclusions

In conclusion, an optical cavity structure with a high Q-factor has been presented, which overcomes the conventional trade-off between optical chirality density and loss in resonant modes, thus providing a new pathway for CD detection. By utilizing a spin-preserving chiral resonator, this structure integrates BIC with GMR and employs a spin-locking mechanism to ensure that the intrinsic chirality of CPL is maintained within the cavity. As a result, both a high Q-factor and an ultrahigh optical chirality density are achieved within a subwavelength-scale localized field. Experimental measurements confirm that the BIC-GMR degenerate state enables nearly perfect TCD, reaching values up to 0.99, without requiring symmetry breaking or changes in the angle of incidence. Full-wave simulations further predict that this synergistically enhanced system can attain a Q-factor as high as 10,037, while generating a localized field within the molecular interaction region where the optical chirality density is enhanced by up to 400 times, ultimately leading to an amplification of the CD signal by more than 5025 times. This study not only lays the foundation for the detection of low-concentration chiral molecules but also reveals a high-Q-factor enhancement mechanism, which is expected to have broad applications in advanced fields such as chiral photonic crystal lasers and in situ monitoring of asymmetric catalysis. The findings presented here are expected to provide significant impetus for the further development of chiral optoelectronic systems, pushing the boundaries of sensitivity and functional integration.

References

1. Ma BJ, Bianco A. Regulation of biological processes by intrinsically chiral engineered materials. *Nat Rev Mater* **8**, 403–413 (2023).
2. Warning LA, Miandashti AR, McCarthy LA et al. Nanophotonic approaches for chirality sensing. *ACS Nano* **15**, 15538–15566 (2021).
3. Mun J, Kim M, Yang Y et al. Electromagnetic chirality: from fundamentals to nontraditional chiroptical phenomena. *Light Sci Appl* **9**, 139 (2020).
4. Spreyer F, Mun J, Kim H et al. Second harmonic optical circular dichroism of plasmonic chiral helicoid-III nanoparticles. *ACS Photonics* **9**, 784–792 (2022).
5. Park J, Noh J, Shin J et al. Investigating static and dynamic behaviors in 3D chiral mechanical metamaterials by disentangled generative models. *Adv Funct Mater* **35**, 2412901 (2025).
6. Tullius R, Karimullah AS, Rodier M et al. "Superchiral" spectroscopy: detection of protein higher order hierarchical structure with chiral plasmonic nanostructures. *J Am Chem Soc* **137**, 8380–8383 (2015).
7. Hendry E, Carpy T, Johnston J et al. Ultrasensitive detection and characterization of biomolecules using superchiral fields. *Nat Nanotechnol* **5**, 783–787 (2010).
8. Tullius R, Platt GW, Khosravi Khorashad L et al. Superchiral plasmonic phase sensitivity for fingerprinting of protein interface structure. *ACS Nano* **11**, 12049–12056 (2017).
9. Kim I, Kim H, Han S et al. Metasurfaces-driven hyperspectral imaging via multiplexed plasmonic resonance energy transfer. *Adv Mater* **35**, 2370224 (2023).
10. Kim I, Kim H, Go M et al. Ultrafast metaphotonic PCR chip with near-perfect absorber. *Adv Mater* **36**, 2311931 (2024).
11. Tang YQ, Cohen AE. Enhanced enantioselectivity in excitation of chiral molecules by superchiral light. *Science* **332**, 333–336 (2011).
12. Jia TX, Li BJ, Zhang ZR et al. Superchirality induced enhanced circular dichroism spectroscopy via multi-beam superposition. *Results Phys* **52**, 106857 (2023).
13. Yao K, Zheng YB. Near-ultraviolet dielectric metasurfaces: from surface-enhanced circular dichroism spectroscopy to polarization-preserving mirrors. *J Phys Chem C* **123**, 11814–11822 (2019).
14. Yao K, Liu YM. Enhancing circular dichroism by chiral hotspots in silicon nanocube dimers. *Nanoscale* **10**, 8779–8786 (2018).
15. García-Guirado J, Svedendahl M, Puigdollers J et al. Enantiomer-selective molecular sensing using racemic nanoplasmonic arrays. *Nano Lett* **18**, 6279–6285 (2018).
16. Hu HF, Zhan QW. Enhanced chiral Mie scattering by a dielectric sphere within a superchiral light field. *Physics* **3**, 747–756 (2021).
17. Tang YQ, Cohen AE. Optical chirality and its interaction with matter. *Phys Rev Lett* **104**, 163901 (2010).
18. Li XT, Cai XD, Liu C et al. Cascaded metasurfaces enabling

adaptive aberration corrections for focus scanning. *Opto-Electron Adv* **7**, 240085 (2024).
19. Tang P, Li XT, Kim Y et al. Spin Hall effect of light in a Dichroic polarizer for multifunctional edge detection. *ACS Photonics* **11**, 4170–4176 (2024).
20. Kim H, Yun H, Jeong S et al. Optical metasurfaces for biomedical imaging and sensing. *ACS Nano* **19**, 3085–3114 (2025).
21. Nesterov ML, Yin XH, Schäferling M et al. The role of plasmon-generated near fields for enhanced circular dichroism spectroscopy. *ACS Photonics* **3**, 578–583 (2016).
22. Kim Y, Kim H, Yang Y et al. Three-dimensional artificial chirality towards low-cost and ultra-sensitive enantioselective sensing. *Nanoscale* **14**, 3720–3730 (2022).
23. Lee YH, Won Y, Mun J et al. Hierarchically manufactured chiral plasmonic nanostructures with gigantic chirality for polarized emission and information encryption. *Nat Commun* **14**, 7298 (2023).
24. Alizadeh MH, Reinhard BM. Plasmonically enhanced chiral optical fields and forces in achiral split ring resonators. *ACS Photonics* **2**, 361–368 (2015).
25. Solomon ML, Hu J, Lawrence M et al. Enantiospecific optical enhancement of chiral sensing and separation with dielectric metasurfaces. *ACS Photonics* **6**, 43–49 (2019).
26. Tseng ML, Jahani Y, Leitis A et al. Dielectric metasurfaces enabling advanced optical biosensors. *ACS Photonics* **8**, 47–60 (2021).
27. Hu J, Lawrence M, Dionne JA. High quality factor dielectric metasurfaces for ultraviolet circular dichroism spectroscopy. *ACS Photonics* **7**, 36–42 (2020).
28. Koshelev K, Favraud G, Bogdanov A et al. Nonradiating photonics with resonant dielectric nanostructures. *Nanophotonics* **8**, 725–745 (2019).
29. Mohammadi E, Tittl A, Tsakmakidis KL et al. Dual nanoresonators for ultrasensitive chiral detection. *ACS Photonics* **8**, 1754–1762 (2021).
30. Jia TX, Li BJ, Gu B et al. Strong coupling induced ultrasensitive chiral detection by metal-dielectric hybrid metasurface. *Opt Laser Technol* **181**, 111995 (2025).
31. Zhao Y, Askarpour AN, Sun LY et al. Chirality detection of enantiomers using twisted optical metamaterials. *Nat Commun* **8**, 14180 (2017).
32. Tanaka K, Arslan D, Fasold S et al. Chiral bilayer all-dielectric metasurfaces. *ACS Nano* **14**, 15926–15935 (2020).
33. Schäferling M, Yin XH, Engheta N et al. Helical plasmonic nanostructures as prototypical chiral near-field sources. *ACS Photonics* **1**, 530–537 (2014).
34. Khoo EH, Leong ESP, Wu SJ et al. Effects of asymmetric nanostructures on the extinction difference properties of actin biomolecules and filaments. *Sci Rep* **6**, 19658 (2016).
35. Biswas A, Cencillo-Abad P, Shabbir MW et al. Tunable plasmonic superchiral light for ultrasensitive detection of chiral molecules. *Sci Adv* **10**, eadk2560 (2024).
36. Rui GC, Hu HF, Singer M et al. Symmetric meta-absorber-induced superchirality. *Adv Opt Mater* **7**, 1901038 (2019).
37. Feis J, Beutel D, Köpfler J et al. Helicity-preserving optical cavity modes for enhanced sensing of chiral molecules. *Phys Rev Lett* **124**, 033201 (2020).
38. Scott P, Garcia-Santiago X, Beutel D et al. On enhanced sensing of chiral molecules in optical cavities. *Appl Phys Rev* **7**, 041413 (2020).
39. Lee J, Jeong M, Jang J et al. Bound-states-in-the-continuum-induced directional photoluminescence with polarization singularity in WS_2 monolayers. *Nano Lett* **25**, 861–867 (2025).
40. Hou YD, Qiu M, Cao ZL et al. High-Q circular dichroism resonances in plasmonic lattices with chiral unit cells. *Adv Funct Mater* **32**, 2204095 (2022).
41. Mur-Petit J, Molina RA. Chiral bound states in the continuum. *Phys Rev B* **90**, 035434 (2014).
42. Tang YH, Liang Y, Yao J et al. Chiral bound states in the continuum in plasmonic metasurfaces. *Laser Photonics Rev* **17**, 2200597 (2023).
43. Droulias S. Chiral sensing with achiral isotropic metasurfaces. *Phys Rev B* **102**, 075119 (2020).
44. Overvig A, Yu NF, Alù A. Chiral quasi-bound states in the continuum. *Phys Rev Lett* **126**, 073001 (2021).
45. Zhang XD, Liu YL, Han JC et al. Chiral emission from resonant metasurfaces. *Science* **377**, 1215–1218 (2022).
46. Shi T, Deng ZL, Geng GZ et al. Planar chiral metasurfaces with maximal and tunable chiroptical response driven by bound states in the continuum. *Nat Commun* **13**, 4111 (2022).
47. Rosas S, Adi W, Beisenova A et al. Enhanced biochemical sensing with high-*Q* transmission resonances in free-standing membrane metasurfaces. *Optica* **12**, 178–189 (2025).
48. Voronin K, Taradin AS, Gorkunov MV et al. Single-handedness chiral optical cavities. *ACS Photonics* **9**, 2652–2659 (2022).
49. Semnani B, Flannery J, Al Maruf R et al. Spin-preserving chiral photonic crystal mirror. *Light Sci Appl* **9**, 23 (2020).
50. Gorkunov MV, Antonov AA, Kivshar YS. Metasurfaces with maximum chirality empowered by bound states in the continuum. *Phys Rev Lett* **125**, 093903 (2020).
51. Kondratov AV, Gorkunov MV, Darinskii AN et al. Extreme optical chirality of plasmonic nanohole arrays due to chiral Fano resonance. *Phys Rev B* **93**, 195418 (2016).
52. Tang F, Wu JJ, Albrow-Owen T et al. Metasurface spectrometers beyond resolution-sensitivity constraints. *Sci Adv* **10**, eadr7155 (2024).
53. Liu TT, Qin MB, Qiu JM et al. Polarization-independent enhancement of third-harmonic generation empowered by doubly degenerate quasi-bound states in the continuum. *Nano Lett* **25**, 3646–3652 (2025).
54. Liu TT, Qiu JM, Xu L et al. Edge detection imaging by quasi-bound states in the continuum. *Nano Lett* **24**, 14466–14474 (2024).
55. Kang L, Rodrigues SP, Taghinejad M et al. Preserving spin states upon reflection: linear and nonlinear responses of a chiral meta-mirror. *Nano Lett* **17**, 7102–7109 (2017).
56. Chen TL, Salij A, Parrish KA et al. A 2D chiral microcavity based on apparent circular dichroism. *Nat Commun* **15**, 3072 (2024).
57. Mohammadi E, Tavakoli A, Dehkhoda P et al. Accessible superchiral near-fields driven by tailored electric and magnetic resonances in all-dielectric nanostructures. *ACS Photonics* **6**, 1939–1946 (2019).
58. García-Guirado J, Svedendahl M, Puigdollers J et al. Enhanced chiral sensing with dielectric nanoresonators. *Nano Lett* **20**, 585–591 (2020).

Acknowledgements

This work was financially supported by the POSCO-POSTECH-RIST Convergence Research Center program funded by POSCO, and the National Re-

search Foundation (NRF) grant (RS-2024-00462912) funded by the Ministry of Science and ICT (MSIT) of the Korean government. This work was also partially supported by National Natural Science Foundation of China (Nos. 12274074, 12134013); Natural Science Foundation of Jiangsu Province (BK20242024); China Scholarship Council (202406090137); Postgraduate Research & Practice Innovation Program of Jiangsu Province (KYCX24_0379). Y. J. acknowledges the NRF Ph.D. fellowship (RS-2025-25437554) funded by the Ministry of Education (MOE) of the Korean government.

Author contributions

T.J. conducted the numerical simulations, participated in the experiments, and prepared the original draft. Y. J. participated in the experiments and prepared the original draft. L. F. and B. L. assisted in data and results analysis. H. K. revised the manuscript. G. R. initiated the idea, revised the manuscript, and supervised the project. J. R. guided the entire work.

Competing interests

The authors declare no competing financial interests.

Supplementary information

Supplementary information for this paper is available at https://doi.org/10.29026/oea.2025.250079

Scan for Article PDF